Progress Towards the Design of a Natural Laminar Flow Wing for a Low-Boom Concept using CDISC

Michael D. Bozeman[*], Richard L. Campbell[†], and Michelle N. Banchy[‡]
NASA Langley Research Center, Hampton, VA, 23681

The X-59 is being developed to evaluate the ability to reduce sonic boom loudness to acceptable levels, with the ultimate goal of enabling supersonic flight overland. If successful, one of the future research challenges will be focused on reducing fuel burn. In this paper, Natural Laminar Flow (NLF) is proposed as a technology to decrease fuel burn for a low-boom configuration. This will require an evaluation of the compatibility of NLF wings for a low-boom configuration. As a first step towards this goal, the CATNLF method was employed using the CDISC design module to perform NLF design on an isolated wing from a low-boom configuration. The results show that the NLF wing features laminar flow over 46% of the wing upper surface, providing a potential 8.3 drag count reduction relative to the design with no laminar flow. Off-design analyses were additionally performed to evaluate the performance of the NLF wing for changes in angle of attack and Mach number. The results showed that the NLF wing offers a performance benefit over the entire range of off-design conditions considered, with most of the laminar flow maintained for near cruise conditions. Future work will consider the full configuration, which will enable an assessment of the impact of the NLF wing design on sonic boom loudness. Additionally, attachment line transition will be addressed, which was predicted to result in a loss of laminar flow on the inboard 50% span for this work. Finally, future research will focus on developing a method for effectively choosing the frequency-beta pairs used for the stability analysis to improve transition prediction and provide a more accurate estimate of the performance benefit.

Nomenclature

Acronyms

AL	=	Attachment Line
BLSTA3D	=	Boundary Layer code for Stability Analysis 3D
CATNLF	=	Crossflow-attenuated Natural Laminar Flow
CDISC	=	Constrained Direct Iterative Surface Curvature
CF	=	Crossflow
FB	=	Frequency-Beta
LASTRAC	=	Langley Stability and Transition Analysis Code
LFC	=	Laminar Flow Control
LST	=	Linear Stability Theory
NF	=	N factor
NLF	=	Natural Laminar Flow
OTS	=	Oblique Tollmien-Schlichting
RANS	=	Reynolds-averaged Navier Stokes
TCF	=	Traveling Crossflow
TS	=	Tollmien-Schlichting

[*]Research Aerospace Engineer, NASA Langley Research Center, Configuration Aerodynamics Branch, AIAA Member.
[†]Senior Research Engineer, NASA Langley Research Center, Configuration Aerodynamics Branch, AIAA Associate Fellow.
[‡]Research Aerospace Engineer, NASA Langley Research Center, Configuration Aerodynamics Branch, AIAA Member.

Symbols

α	=	angle of attack, degrees
C_D	=	drag coefficient
$C_{D,pressure}$	=	pressure (inviscid) component of drag coefficient
$C_{D,viscous}$	=	viscous component of drag coefficient
C_L	=	lift coefficient
c_l	=	sectional lift coefficient
$C_{L,design}$	=	design lift coefficient
c_m	=	sectional pitching moment coefficient
η	=	nondimensional spanwise location
Λ_{LE}	=	leading-edge sweep, degrees
M_∞	=	freestream Mach number
Re_c	=	Reynolds number based on local chord
Re_{MAC}	=	Reynolds number based on mean aerodynamic chord
Re_T	=	transition Reynolds number
Re_θ	=	Reynolds number based on boundary layer momentum thickness
$(r/c)_{LE}$	=	leading-edge radius normalized by local chord
$(t/c)_{LE}$	=	maximum thickness normalized by local chord
x, y, z	=	coordinate axes
x_1	=	streamwise location to end rapid flow acceleration normalized by local chord
x_3	=	streamwise location to end rooftop gradient normalized by local chord
y^+	=	dimensionless wall spacing

I. Introduction

The future of supersonic aviation depends on the ability to reduce sonic boom loudness to acceptable levels. As a step towards this goal, NASA's Quesst project is focused on the design of a low-boom, supersonic transport aircraft, designated as the X-59, to demonstrate the ability to design a low-boom aircraft, evaluate our computational prediction capabilities, and establish acceptable loudness levels. If successful, future challenges will include airport noise considerations and aircraft performance. Natural Laminar Flow (NLF) wings are a fuel burn reduction technology that could benefit supersonic transports. NLF wings are designed to provide laminar flow over a portion of the wing, which offers a reduction in drag due to the smaller skin friction penalty associated with a laminar boundary layer. However, the compatibility of pressure distributions and geometry characteristics required for NLF with a low-boom configuration is unknown. This paper discusses research performed as a preliminary step towards identifying this compatibility.

For supersonic flight, there are four types of boundary layer transition mechanisms that need to be addressed in order to sustain laminar flow: attachment line (AL) contamination/transition, Görtler vortices, bypass transition, and modal disturbances [1]. AL contamination refers to the occurrence of a turbulent fuselage boundary layer impacting the leading edge due to wing sweep. This can result in transition and, potentially, a total loss of laminar flow. There are various methods to address AL contamination and transition. One method is the application of a Gaster bump [2], which can prevent transition caused by AL contamination by diverting the fuselage turbulent boundary layer away from the leading edge. Another notable method involves designing the leading-edge radius based on the application of Poll's criterion [3]. Poll's criterion states that AL contamination may occur for $100 \leq Re_\theta < 235$ and AL transition will occur when $Re_\theta \geq 235$, where Re_θ is the Reynolds number based on boundary layer momentum thickness. Typically, AL contamination and transition can be mitigated by lowering Re_θ through reductions in the leading-edge radius or reducing wing sweep. Note that AL contamination/transition is not considered in this work but will be addressed in future research. Görtler vortices can also potentially cause boundary layer transition, which are counter-rotating vortices that can be present in regions of concavity on the wing surface. For this work, transition induced by Görtler vortices was prevented by enforcing curvature constraints to force surface convexity in regions where laminar flow is desired

and/or expected. Bypass transition can occur due to surface imperfections, such as steps, gaps, and/or fasteners. This transition mode is primarily addressed during manufacturing and maintenance. For NLF design, bypass transition can be accounted for by limiting laminar flow extents based on expected surface imperfections (e.g., control surface gaps). This work partially accounts for bypass transition concerns by limiting laminar flow to the upper surface only. Future research will additionally account for the presence of control surfaces. Finally, the modal disturbances known to cause boundary layer transition include crossflow (CF) waves, Tollmien-Schlichting (TS) waves, traveling crossflow (TCF) waves, and oblique Tollmien-Schlichting (OTS) waves. The TCF and OTS modes are variations of TS and CF modal disturbances specific to supersonic applications. These modal disturbances are discussed further in Section III.D.

Supersonic aircraft typically feature highly swept wings, which can pose significant challenges for NLF design. Swept wings are more susceptible to CF, and TCF for supersonic applications, induced transition. These modes are dominant in the leading-edge region and, therefore, are critical to suppress since they would lead to a loss of laminar flow over the full chord at that spanwise location. Historically, CF and TCF modes have been suppressed by limiting leading-edge sweep to 20 degrees or less for NLF applications. However, supersonic applications generally require leading-edge sweeps significantly greater than 20 degrees to limit wave drag penalties. Figure 1 illustrates the current empirical boundary for NLF as a function of leading-edge sweep (Λ_{LE}) and Reynolds number based on streamwise transition location (Re_T). The NLF boundary is currently defined by flight data obtained for the F-14 Variable Sweep Flight Transition Experiment (VSFTE) configuration, which represents the largest published combinations of Re_T and Λ_{LE} [4]. On the other side of the NLF boundary is laminar flow control (LFC), which can provide larger combinations of Re_T and Λ_{LE}. LFC methods typically employ suction at the leading edge to suppress CF modes. However, LFC applications increase both system complexity and weight, which reduces the benefit offered by laminar flow. The present work employs the Crossflow-ATtenuated Natural Laminar Flow (CATNLF) [5, 6] method to suppress CF modes by designing to sectional pressure targets featuring a rapid leading-edge acceleration. The CATNLF method can provide NLF for configurations with sweep that exceeds the boundary shown in Figure 1 without the penalties and cost associated with LFC. While the majority of the CATNLF applications to date have been focused on the transonic flow regime, previous work applied the method to a supersonic configuration, the NASA-JAXA Wing Body (NJWB) [7]. The NJWB NLF wing design featured laminar flow over 40% of the wing upper surface for a wing with combination of Λ_{LE} and Re_T as large as 72 degrees and 36 million. The results showed a 4.3 count reduction in drag coefficient, for an overall 5% reduction in drag. This work provides an example of the ability to obtain NLF for a supersonic configuration with a highly swept leading edge.
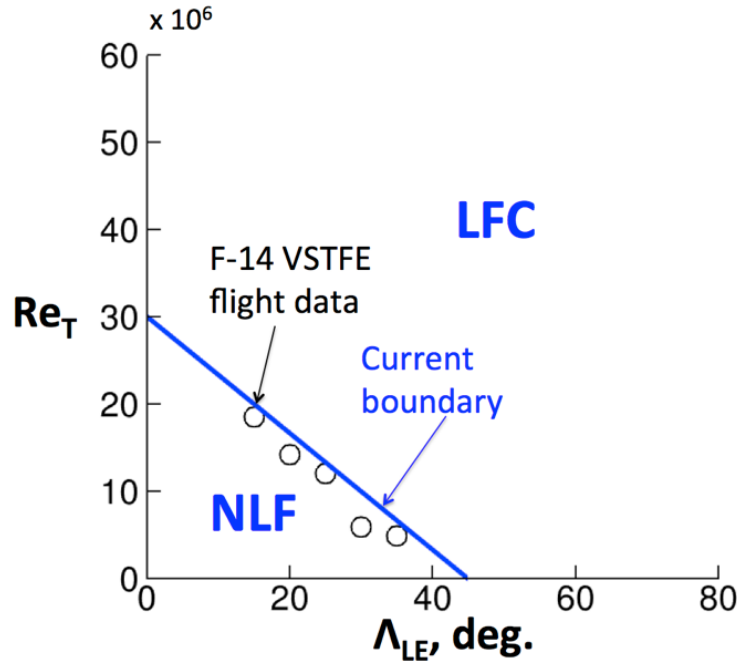

Figure 1. Empirical boundary for Re_T and Λ_{LE} combinations that enable NLF.

The goal of the present research is to perform NLF design for a low-boom configuration to enable an assessment of the impact of the CATNLF pressure target architecture on the sonic boom loudness. As a first step towards this goal, the Constrained Direct Iterative Surface Curvature (CDISC) method was used to perform a preliminary design study for an isolated wing from an early variant of the X-59. CDISC is a knowledge-based design tool that performs airfoil shape changes at discrete spanwise stations based on pressure targets defined by empirical data and/or user inputs. For this work, the CATNLF method was employed to define the pressure targets required to achieve NLF. The CDISC and CATNLF methods are discussed further in Sections III.C and III.E. The results of the preliminary design study are discussed in this paper. Additionally, future work is discussed to provide insight into the next steps.

II. Geometry

The goal is to assess the potential benefit of NLF for a supersonic transport and to investigate the compatibility with low boom. As a first step towards this goal, a design study was performed considering an isolated wing from the C607 concept. The C607 is an early iteration of the X-59 configuration that was tested in the 8x6-foot Supersonic Wind Tunnel at the NASA Glenn Research Center [8]. This geometry was selected because it is a low-boom, supersonic concept that was readily available and was not restricted for publication. Note that all control surfaces were removed from the wing for this preliminary study. An illustration of the simplified C607 wing geometry is provided in Figure 2.
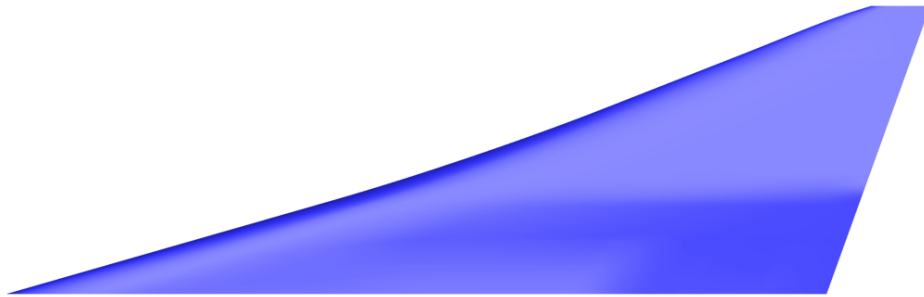
Figure 2. C607 (Simplified) Wing Geometry.

The simplifications discussed here allow for the design methods to be established and evaluated for the supersonic transport problem while reducing computational cost and simplifying grid movement, especially near the wing-fuselage juncture. However, limiting the design study to the isolated wing prevents the ability for an assessment of the compatibility of NLF with low boom. Also, the extent of laminar flow could be over-exaggerated due to the lack of integration effects and the removal of the control surfaces, which will limit the extent of laminar flow that can be achived. These considerations will be addressed in future research.

III. Design Methods

This section discusses the tools and methods employed for this work. The discussion includes descriptions of the grid generation, CFD method, design module, and stability analysis. Additionally, a description of the CATNLF design method employed to define the sectional pressure targets is provided.

A. Grid Generation

The computational grid was generated using HeldenMesh^{TM} v3.08 grid generation software. HeldenMesh^{TM} is an unstructured grid generator that is part of a software suite developed by the Helden Aerospace Corporation. It utilizes multi-threading for the rapid generation of both tetrahedral and mixed-element grids. HeldenMesh^{TM} allows the user to specify the desired resolution of the surface grid through a series of inputs including base spacing, minimum spacing, edge spacing, and maximum surface deviation. This process is fairly automated depending on the complexity of the geometry as well as the user preferences. HeldenMesh^{TM} uses cell stretching to resolve surface curvature with anisotropic triangles. The user can control the degree of anisotropy through the maximum aspect ratio definition. HeldenMesh^{TM} utilizes tetrahedral or prismatic elements to resolve the boundary layer based on a user-specified growth

rate, number of layers, and initial wall spacing. Finally, the remaining volume is filled with tetrahedral elements, with pyramidal elements as necessary to provide transitions from prismatic to tetrahedral elements.

For this work, a grid was generated for the semispan C607 wing. An illustration of the grid is shown in Figure 3. The initial wall spacing was defined based on a desired y^+ of 1 at the design flight condition; Re_{MAC} = 33 million and M_∞ = 1.4. NLF design using CDISC requires adequate grid refinement along the leading edge. This requirement is to provide accurate prediction of the leading-edge acceleration prescribed by the CATNLF design method, which will be discussed in Section III.E, and to provide an accurate representation of the surface curvature for accurate leading-edge radius calculations. The current best practice is to apply a leading-edge spacing of ≤1% of the local chord. Preliminary design studies showed the occurrence of undulations in the pressure distribution near the leading edge, that correlated with significant gradients in cell size. These features were observed in solutions from early designs and caused early transition. Based on this finding, the wing was prescribed a relatively uniform cell size distribution, as opposed to the cell size correlating with local curvature. This change was shown to improve the smoothness of the pressure distribution and will be a grid generation best practice for the design of NLF wings moving forward.

(a) Leading edge.

(b) Symmetry plane at y = 0.

(c) Upper surface.
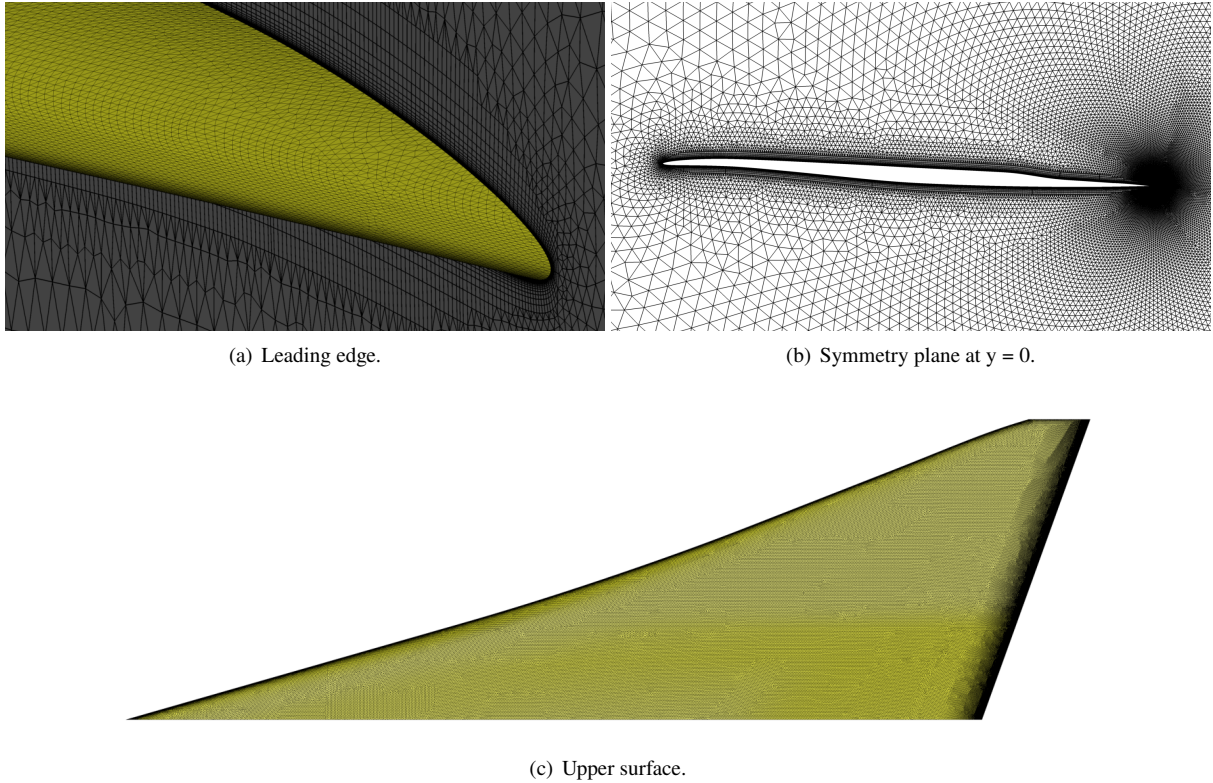
Figure 3. Mixed-element grid generated for the C607 wing.

B. Flow Solver

The mixed-element USM3D (USM3D-ME) flow solver was used for this work, which is an extension of the legacy USM3D flow solver. USM3D is an unstructured-grid, cell-centered, Navier-Stokes solver developed at the NASA Langley Research Center as part of the Tetrahedral Unstructured Software System (TetrUSS) [9, 10]. Compared to the legacy version of the code, USM3D-ME offers compatibility with mixed-element grids featuring tetrahedral, prismatic, pyramidal, and hexahedral elements [11] along with other enhancements to improve robustness and time to solution. One significant enhancement included with USM3D-ME is the Hierarchical Adaptive Nonlinear Iteration Method (HANIM), which has been shown to be beneficial for some problems through improved robustness, accelerated convergence, and automation [12]. The automation offered by HANIM includes a Courant-Friedrichs-Lewy (CFL) number adaptation capability, which automatically adjusts the CFL number based on the current state of the solution. This can potentially increase the convergence rate and does not require CFL input from the user. For this work, the inviscid terms were

computed using Roe's flux difference splitting [13] without a flux limiter. The method for turbulent closure was the one-equation Spalart-Allmaras model with negative provisions [14]. The forced laminarization capability available in USM3D-ME was utilized to assess the performance benefit for a user-prescribed transition front. Finally, HANIM was used for all simulations presented in this paper.

C. Design Module

To perform the NLF wing design, the USM3D-ME flow solver was coupled with the CDISC design module [15]. CDISC has been used extensively for both NLF and turbulent designs at transonic and supersonic flight conditions [7, 16]. It alters the geometry to achieve target pressure distributions at discrete design stations, where the geometry changes are based on flow-geometry sensitivity derivatives prescribed from empirical data and/or analytical studies. CDISC allows the user to specify flow constraints corresponding to a variety of engineering design variables, such as span load, sectional force and moment coefficients, shock location, and shock strength. Similarly, geometry constraints are available to address requirements from other disciplines such as structures and manufacturing, including thickness, curvature, volume, and leading-edge radius. For NLF applications, the CATNLF pressure architecture algorithm is built into CDISC to automatically generate target pressure distributions that support laminar flow.

D. Transition Prediction Tools

The boundary layer stability analysis and transition prediction were performed using BLSTA3D (Boundary Layer code for Stability Analysis 3D) [17] and LASTRAC (Langley Stability and Transition Analysis Code) [18]. Boundary layer profile information is calculated from streamwise pressure distributions using the conical flow assumption at several stations on the wing by the BLSTA3D code. BLSTA3D also calculates the Reynolds number based on the attachment line boundary layer momentum thickness, Re_θ, to enable evaluation of the attachment line state. The resulting boundary layer profiles are used to perform stability analyses in LASTRAC, which calculates the growth of relevant modal instabilities. As discussed in Section I, there are four modal instabilities that are relevant for supersonic applications, which are illustrated in Figure 4 as a function of frequency and spanwise wave number (beta). Note that for this work, OTS and TCF are lumped together into a single mode designated as FB (frequency-beta).
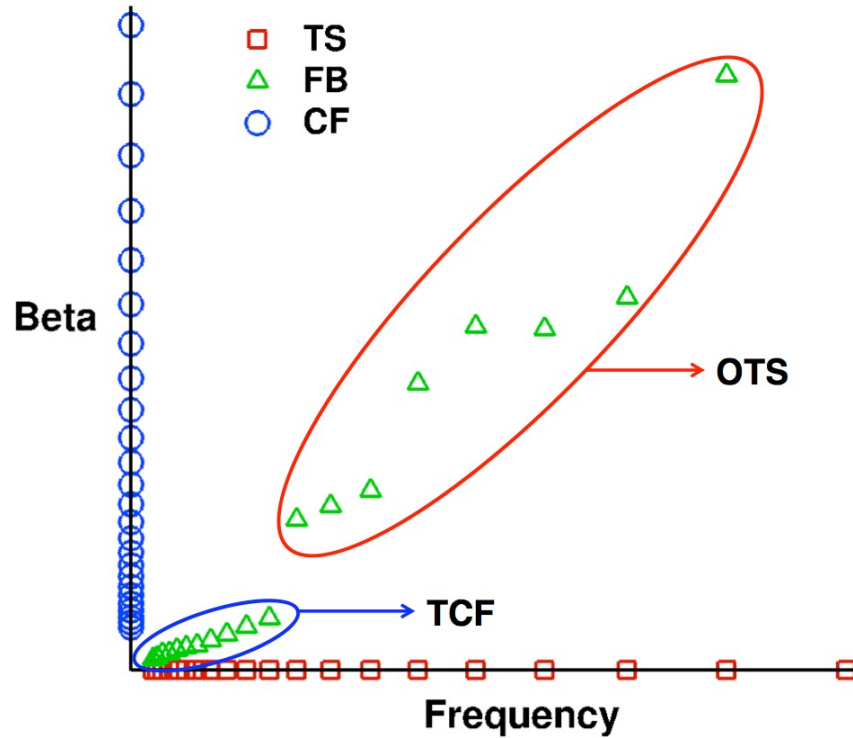

Figure 4. Critical transition modes for supersonic applications.

The modal instabilities shown in Figure 4 are associated with boundary layer eigenmodes and each responds differently to pressure gradients (stabilizing or destabilizing). The instabilities may propagate and amplify, ultimately leading to transition in different regions over the wing. LASTRAC performs a linear stability analysis, based on Linear Stability Theory (LST), for twenty combinations of frequency and beta, which are calculated for each station based on the local flow and geometry. Compressibility effects are also included in the stability analysis. Note that surface curvature effects are not included. LASTRAC predicts the growth of TS, CF, and FB modal instabilities, where transition is predicted to occur either when the growth of one or more modal instabilities exceeds the user-defined critical N factor (NF) or when the pressure gradient exceeds an internal criteria for the existence of a laminar boundary layer. For this work, the critical N factor was chosen to be 10, which is representative of a flight environment.

E. Design Approach

This work employs the CATNLF design approach, which consists of designing to sectional pressure targets featuring rapid acceleration at the leading edge to mitigate CF and leading-edge FB instabilities followed by a tailored pressure gradient to control TS and mid-chord FB instabilities. The general idea is to use the CATNLF methodology to define sectional pressure targets at discrete, spanwise design stations. The pressure target definitions used in CDISC require three user inputs: x_1, the universal damping factor (UDF), and x_3, which correspond to the chordwise location to end the rapid acceleration, the rooftop pressure gradient, and the chordwise location to end the rooftop gradient, respectively. An example pressure target for the C607 wing is shown in Figure 5. The x_1 value can either be specified directly by the user or it can be calculated internally by CDISC to limit CF growth to a maximum of 2-3 units below the critical NF value.
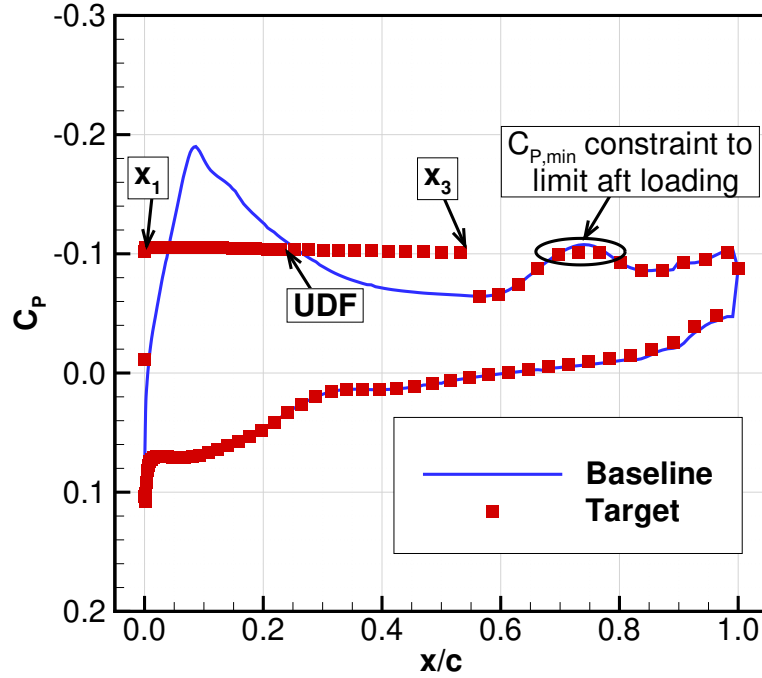

Figure 5. Example target pressure distribution for the C607 wing design.

For this work, x_1 was calculated internally by CDISC, which prevented CF induced transition at all stations. The process for setting UDF and x_3 was more involved. For transonic flow applications, UDF is chosen to tailor TS growth and x_3 generally corresponds to the upper surface shock location. However, supersonic flow applications also have to mitigate FB instabilities, which opposes the suppression of TS. Additionally, given the potential lack of strong shocks on the upper surface for supersonic applications, there may not be a natural location to end the rooftop gradient. Based on these considerations, the UDF and x_3 values were chosen to maximize laminar extent at each design station, which required assessing the impact of UDF and x_3 values on the LASTRAC predicted transition location. The UDF value was chosen to balance TS and FB instabilities, which consisted of finding a value that results in TS- and FB-induced

transition to occur at the same chordwise location. This was performed by varying the UDF parameter in CDISC to generate target pressure distributions. Then, LASTRAC was used to perform a linear stability analysis of the targets. The process was repeated until TS and FB were balanced, transition was limited by the pressure gradient criteria in LASTRAC, and/or transition was not predicted to occur at each design station. Then, for the given UDF value, x_3 was varied to assess the impact on the predicted transition location. For some stations, x_3 could be placed as far back as 99% chord, however moving x_3 too far back actually pushed transition upstream for other stations. From this study, the x_3 value that resulted in the most laminar flow extent at each station was selected for the targets. Downstream of x_3, CDISC defaulted the pressure target values to the current values with a minimum pressure constraint to limit aft loading, as shown in Figure 5. The minimum pressure constraint was added during the design process based on observations of excessive aft loading at some design stations, especially during early design cycles.

For geometry constraints, only three constraints were employed for this work. The leading-edge radius was set to be 0.1% of the local chord, which was found to provide the desired rapid acceleration at the leading edge without a significant overshoot in pressure. Additionally, the upper surface curvature was restricted to be positive between x/c = 0.02 and 0.6 to prevent both unrealistic airfoil shapes and Görtler vortices. The spanwise distribution of maximum thickness-to-chord ratio was constrained to the baseline values. Finally, flow constraints were imposed to maintain the baseline sectional lift and pitching moment coefficient distributions.

F. Procedure

An illustration of the process and tools used for this work is provided in Figure 6. The flow chart illustrates two paths: a design loop and a transition prediction loop. For the design loop, an initial solution is generated for the unmodified geometry using USM3D-ME. The flow solution and geometry at each design station defined in the CDISC input file are extracted and used as inputs to CDISC. CDISC evaluates the difference between the predicted sectional pressure distributions and the targets, and modifies the airfoil geometry at each station. To ensure a smooth wing geometry, CDISC interpolates the airfoil geometry updates between stations and, if desired, extrapolates inboard and outboard. The updates are then used to modify the grid and the next design cycle begins. On the left-hand side, the extracted data from the flow solution is passed to BLSTA3D and LASTRAC to perform transition prediction. This process is performed after a design is completed and typically requires multiple iterations. The first iteration involves extracting the sectional data from a fully turbulent simulation and performing the transition prediction to obtain the transition coordinates. The transition coordinates are then passed to USM3D-ME to perform a forced-laminarization simulation. The laminar boundary layer typically results in a change in the lift coefficient, which requires an angle of attack adjustment to match the lift coefficient for the fully turbulent results and enable drag coefficient comparisons. The angle of attack adjustment can alter the pressure distribution and an updated stability analysis is needed. This process is repeated until the transition front is converged.
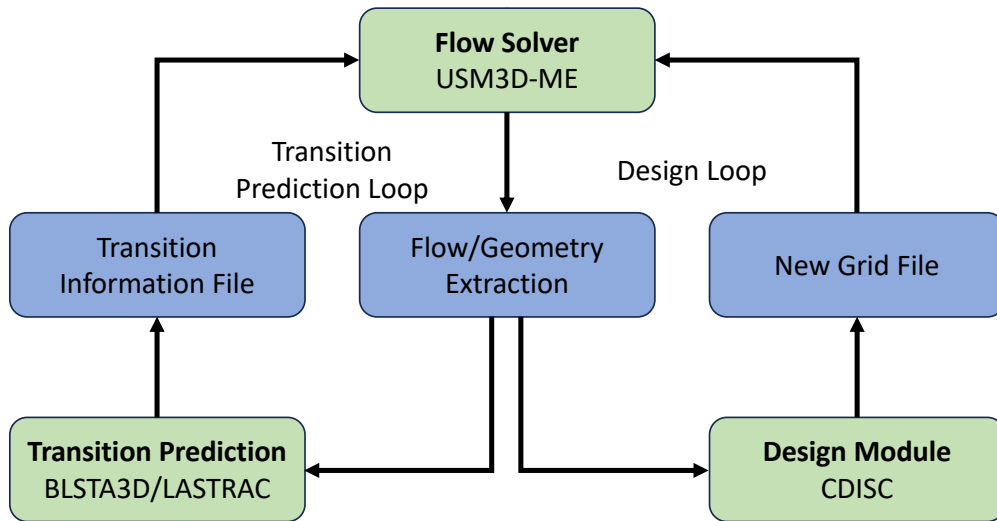

Figure 6. NLF design process and tools.

IV. Results

The C607 wing was divided into 12 design stations for this study, as illustrated in Figure 7. Note that design was not performed directly for stations 1 and 12 to prevent grid movement and blending issues at the root and tip of the wing. However, design was performed indirectly at stations 1 and 12 by copying and scaling the resulting airfoils at stations 2 and 11 each design cycle to provide smooth geometry changes near the root and tip.
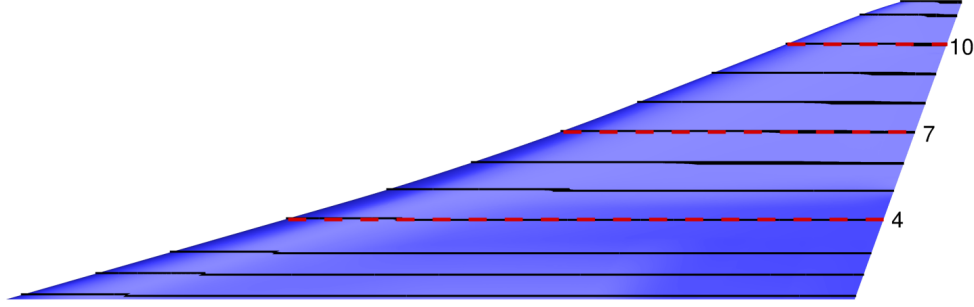

Figure 7. C607 wing with 12 design stations.

A. NLF Design

The NLF design of the C607 wing was performed for a cruise condition corresponding to Re_{MAC} = 33 million, Mach = 1.4, and α = 2.15°. In this subsection, select design results are provided for stations 4, 7, and 10, which are shown as the red dashed lines in Figure 7. These stations correspond to spanwise locations of η = 0.27, 0.56, and 0.86, leading-edge sweep angles of 73.9, 70.0, and 68.5 degrees, and were chosen to illustrate the wing design over the span. The NLF design pressure coefficient distributions and airfoil geometries are compared to the baseline C607 wing in Figure 8 for the three example stations.

The pressure coefficient comparisons provided in Figure 8 illustrate favorable agreement between the NLF design and the targets. Comparing to the baseline results, the NLF design pressure coefficient distributions exhibit the characteristics described in Section III.E, namely a rapid acceleration followed by a relatively flat rooftop. For stations 4 and 7, the combination of the CATNLF criteria and loading constraints require the suction peak to be reduced and pushed forward. The result is a more uniform chordwise loading relative to the baseline configuration. The corresponding airfoil sections show a reduction in leading-edge radius, which helps to achieve the rapid initial acceleration with a sharp corner. Additionally, the maximum thickness is shifted aft to reduce forward loading and provide the desired rooftop gradient. For station 10, the aerodynamic loading across the chord for the baseline configuration was observed to be relatively uniform. The rapid acceleration at the leading edge was achieved with a leading-edge radius larger than the baseline. Also, the maximum thickness is pushed forward for this station to provide the increase in forward loading needed. Note that there are two pressure spikes that show up on the lower surface at station 7. During the wing geometry simplification performed for this study, a coons patch was used to loft over three small bumps on the lower surface. It was later discovered that this created a slight discontinuity in the surface geometry, which shows up in the predicted pressure coefficient. Future work will address these surface discontinuities. However, they are also present in the baseline configuration and do not impact the comparisons discussed in this paper.

The stability analysis results shown in Figure 9 illustrate the growth of the TS, CF, and FB transition modes for both the NLF design and the targets. The results show that CF is sufficiently suppressed by the chosen pressure targets for the three stations shown. This observation was true for all design stations. The selected stations illustrate the three modes of transition observed. Station 4 transitions due to TS growth, station 7 due to FB growth, and station 10 did not transition from either TS or FB growth. Station 10 transitions at 97% chord due to an adverse pressure gradient upstream of the trailing edge that exceeds the LASTRAC criteria for the existence of a laminar boundary layer. Comparing the targets to the NLF design, the targets for station 4 were balanced, with TS and FB both reaching the critical N-factor at 50% chord. However, the NLF design results at station 4 show transition due to TS at 42% chord.
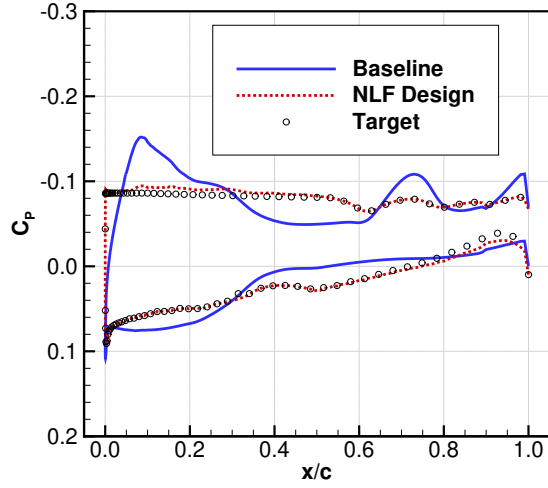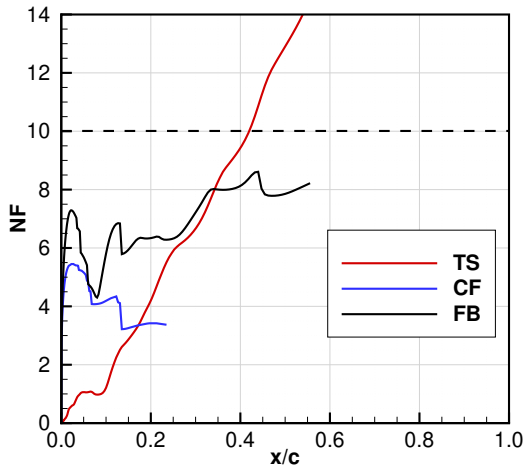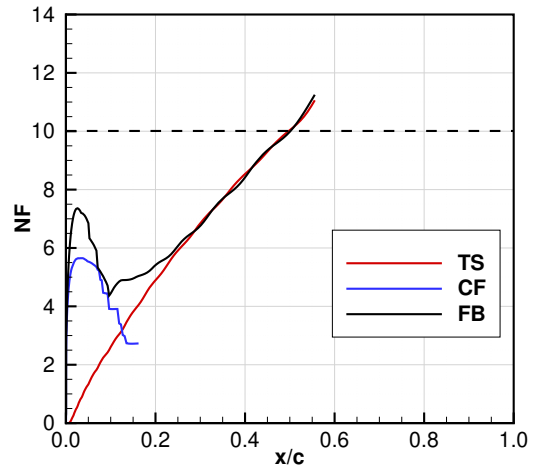
(a) Station 4.
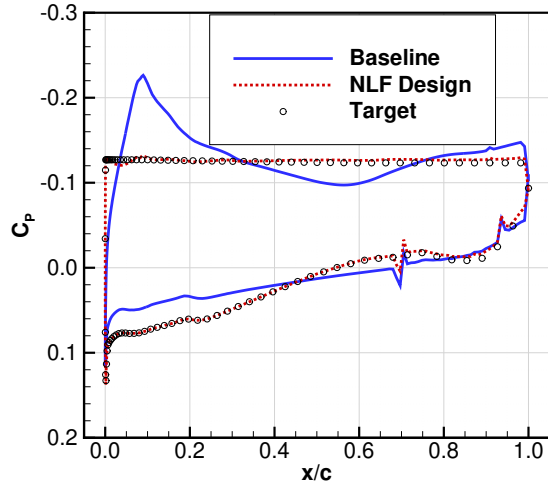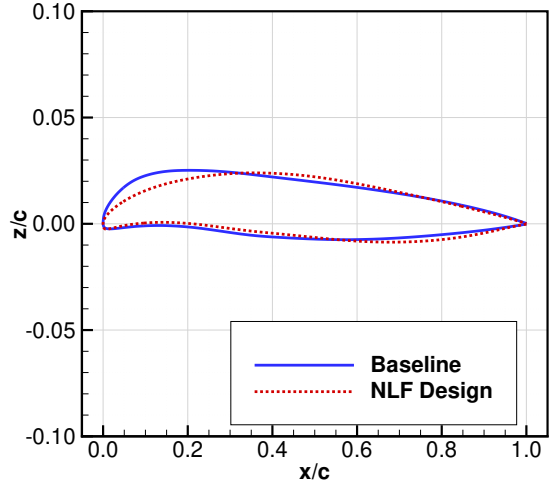
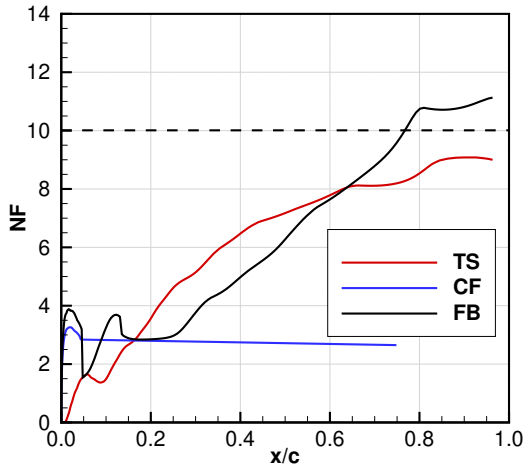(b) Station 7.
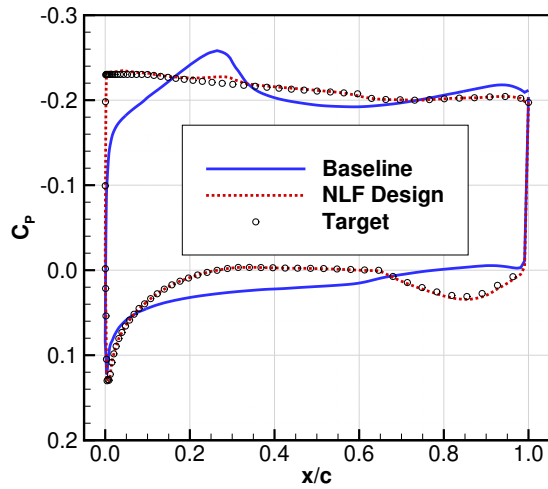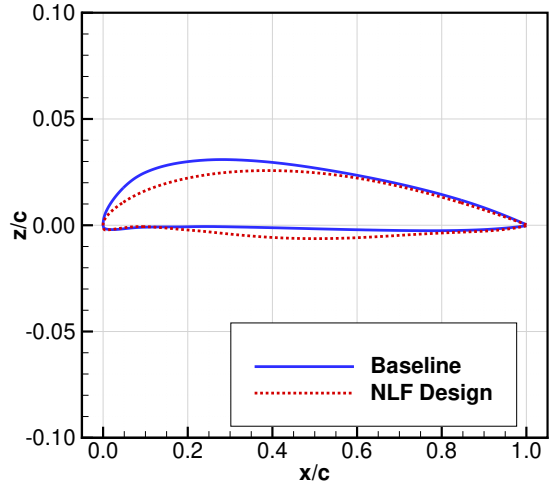
(c) Station 10

Figure 8. Pressure coefficient (left) and geometry (right) comparisons for stations 4, 7, and 10.
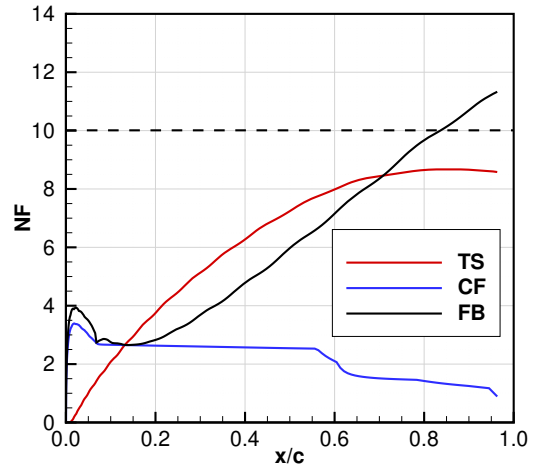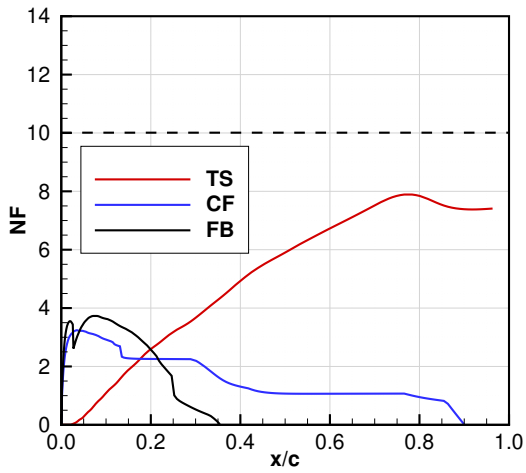
(a) Station 4, design.
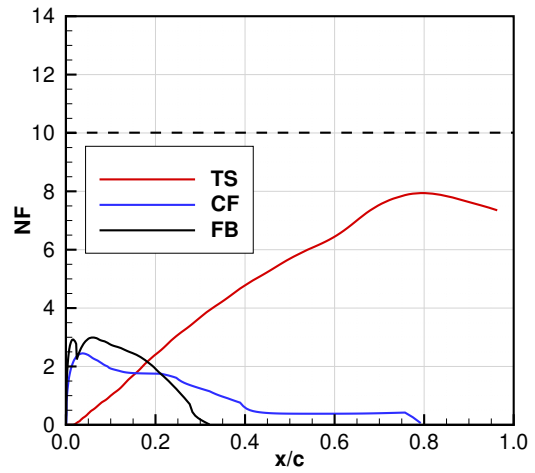
(b) Station 4, target.

(c) Station 7, design.

(d) Station 7, target.

(e) Station 10, design.

(f) Station 10, target.

Figure 9. Growth of TS, CF, and FB modes for both the design (left) and targets (right) at stations 4, 7, and 10.

The pressure coefficient comparisons provided in Figure 8 show the most notable disagreement between the design and targets at station 4, where the NLF design pressure coefficient is more negative than the targets from roughly 5 to 35% chord. This disagreement results in suppression of FB growth near 35% chord and an increase in the slope of TS. Ultimately, this leads to transition occuring forward of the targets by roughly 8% chord. Similarly, NLF design pressure coefficient results for Station 7 show favorable pressure gradient aft of 40% chord compared to the target, which do not feature a pressure gradient on the upper surface in this region. This leads to an increase in slope of FB and transition is pushed forward from 83% to 77% chord, which is a loss of 6% chord. Finally, slight differences are observed between the design and targets at station 10, but both predict transition to occur at 97%. Note that, in reality, the presence of control surfaces would limit the extent of laminar flow that can be achieved. This constraint will be considered in future research.

Spanwise distributions of various design parameters are provided in Figure 10. The sectional lift and pitching moment coefficient comparisons are shown in Figures 10a and 10b, which illustrate favorable agreement between the design and the baseline configuration. Both sectional lift and pitching moment coefficients show the largest differences, relative to the baseline, over the first 50% span. These differences, though minor, are due to challenges achieving the target pressure distributions, which was more common inboard. The leading-edge radius, $(r/c)_{LE}$, was constrained to 0.1% of the local chord for the entire span, as illustrated in Figure 10c. Note that the design features an increase in $(r/c)_{LE}$ both inboard and outboard while a reduction in $(r/c)_{LE}$ is observed mid-span, relative to the baseline. The spanwise twist distribution is shown in Figure 10d, which shows positive twist inboard for the design. This is the region where the pressure targets were most difficult to achieve, leading to more significant geometry changes. The maximum thickness to chord ratio, $(t/c)_{max}$, was constrained to the baseline value for this study, which is confirmed in the results shown in Figure 10d for stations 2 through 11. Note differences at stations 1 and 12 where the airfoils were swapped with the geometry at stations 2 and 11. For station 1, $(t/c)_{max}$ is consistent with station 2. However, $(t/c)_{max}$ at station 12 is slightly larger than observed at station 11, even though the geometry was copied and scaled from station 11. This difference is also observed in $(r/c)_{LE}$ at station 12, which is a function of $(t/c)_{max}$. The difference is because CDISC scales the airfoil by the local chord and trailing edge thickness when copying geometry from another station. For this geometry, the airfoils outboard are relatively thin compared to the thickness of the trailing edge. The result is a slight increase in max thickness at station 12 relative to station 11. However, the difference is less than 1% and due to the smaller chord at station 12, the thickness still decreases moving outboard from station 11 to the wing tip.
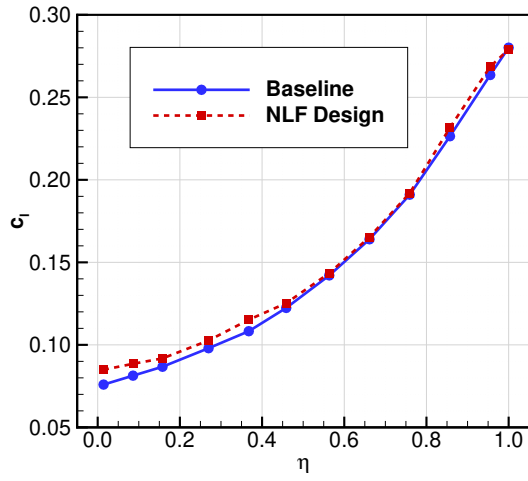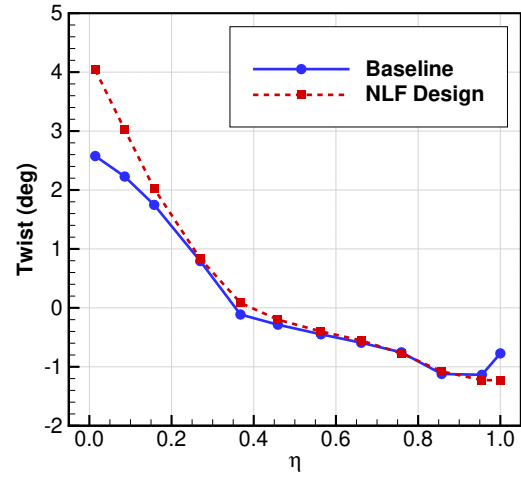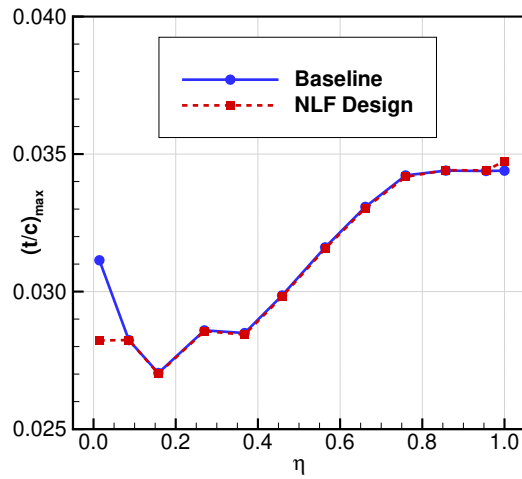
(a) Sectional lift coefficient, c_l.
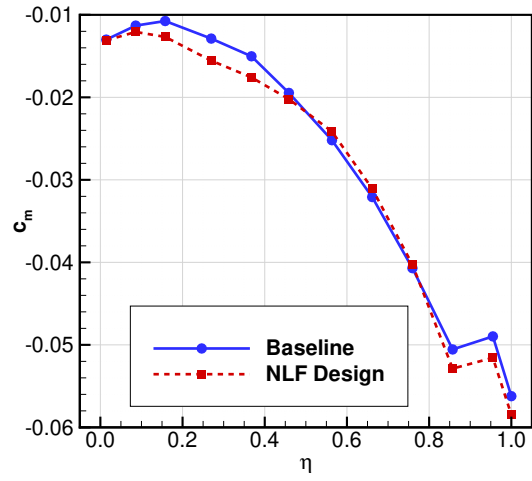
(b) Sectional pitching moment coefficient, c_m.
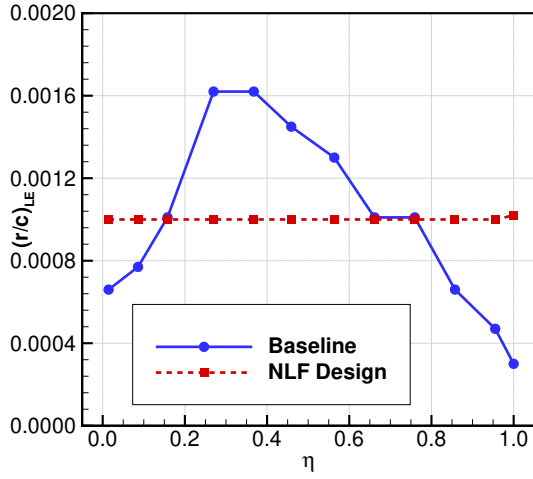
(c) Leading-edge radius, $(r/c)_{LE}$.

(d) Twist (deg).

(e) Maximum thickness-to-chord ratio, $(t/c)_{max}$.

Figure 10. Spanwise comparisons between the design and baseline.

The resulting transition front was obtained from the stability analyses performed at each design station. Figure 11 provides a comparison between the laminar front predicted from the design results and the target. Also, the details of the transition fronts for both the design and targets are provided in Table 1. Note that the target front only extends from station 2 to 11 since stations 1 and 12 were not designed in this study. The results illustrate the challenges with obtaining laminar flow inboard, where the local Reynolds number is the largest. Moving outboard, the chordwise extents of laminar flow are shown to increase, with stations 9 and 10 featuring laminar flow for nearly the entire chord (97% chord). The results show that the NLF design features laminar flow over roughly 46% of the upper surface compared to the target of 54%.
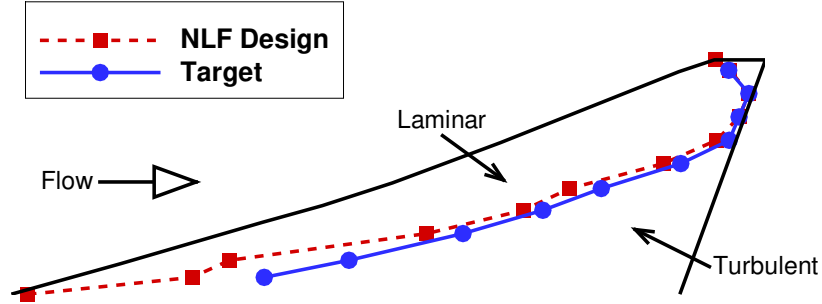
Figure 11. Laminar front comparison between the design and target.

Table 1. Transition front details for both the design and target.

Station	1	2	3	4	5	6	7	8	9	10	11	12
η	0.01	0.09	0.16	0.27	0.37	0.46	0.56	0.66	0.76	0.86	0.95	1.00
Chord (ft)	3.26	3.00	2.74	2.33	1.98	1.69	1.39	1.13	0.88	0.63	0.38	0.24
Re_c (millions)	51.62	47.49	43.37	36.93	31.39	26.76	21.92	17.82	13.87	9.94	6.02	3.82
Λ_{LE}	74.0	74.0	74.0	73.9	73.0	71.5	70.0	68.9	68.6	68.5	70.9	71.8
Design $(x/c)_t$	0.02	0.20	0.18	0.42	0.54	0.57	0.77	0.92	0.97	0.97	0.60	0.00
Target $(x/c)_t$	-	0.31	0.39	0.50	0.59	0.66	0.84	0.97	0.97	0.97	0.59	-

To assess the drag savings provided by the NLF design, the laminar front defined in Table 1 was used perform a forced-laminarization simulation in USM3D-ME. This allows for a prediction of the skin friction benefits offered by the laminar flow. Note that all cases were lift-matched to $C_{L,design}$ = 0.107 to enable consistent comparisons. Additionally, a fully turbulent simulation was performed for the NLF design to assess performance in the case of a total loss of laminar flow. The predicted drag coefficients are compared to the baseline in Table 2.

Table 2. Performance comparison for the C607 NLF wing design at $C_{L,design}$ = 0.107.

	C_D (counts)	$C_{D,viscous}$ (counts)	$C_{D,pressure}$ (counts)
Baseline	99.5	38.5	61.0
NLF Design	87.9	30.8	57.1
NLF Design, Fully Turbulent	96.2	38.3	57.9

Comparing the NLF design performance for the forced-laminarization and fully turbulent cases, the laminar results show an 8.3 count reduction in the drag coefficient. The primary reduction is observed in the viscous component because of the laminar boundary layer over 46% of the upper surface. Note that the baseline performance is also provided in Table 2. However, it was designed for low-boom and not necessarily for optimal performance. This could over-exaggerate the performance benefit relative to a wing designed for performance. Therefore, the comparison to the

baseline is only provided for informational purposes to give the reader an idea of the relative change in performance. Future work will include a fully-turbulent design to provide a better performance comparison.

B. Off-Design Performance

The off-design performance was evaluated to assess the impact of deviations from the design condition, in terms of angle of attack and Mach number changes, on the performance of the NLF design. To perform this assessment, a drag polar was generated by simulating an angle of attack sweep ranging from 1.15° to 3.15° in 0.25° increments, which is a variation of ±1° about the design angle of attack. Similarly, the impact of Mach number was assessed by performing simulations over a range of Mach number of 1.3 to 1.5, ±0.1 about the cruise Mach number, in increments of 0.05. The results of the off-design assessments are provided in the following subsections.

1. Drag Polar

The drag polar results are shown in Figure 12a for the NLF design, both with laminar flow and fully turbulent. Additionally, the drag count reduction between the laminar and fully turbulent solutions is plotted against C_L in Figure 12b to illustrate the performance benefit over the given angle of attack range. In both plots, $C_{L,design}$ and ±10% $C_{L,design}$ are labeled for reference. The NLF design provides a minimum of 1 drag count reduction over the entire range relative to the fully turbulent results, with a reduction of 8.3 counts at the design condition.

(a) Drag polar.

(b) Drag count reduction.
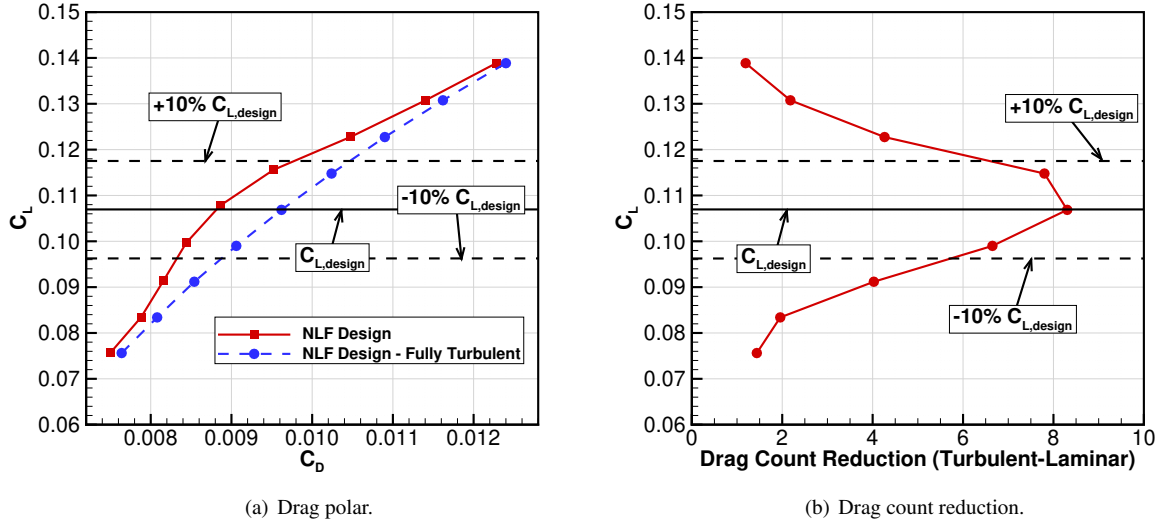
Figure 12. Angle of attack sweep results for the NLF design simulated both with laminar flow and fully turbulent.

The predicted laminar fronts $C_{L,design}$ and ±10% $C_{L,design}$ are illustrated in Figure 13. The results show that the majority of laminar flow is maintained for the ±10% $C_{L,design}$ conditions. The laminar front is shifted forward for the majority of the span for the -10% $C_{L,design}$ front relative to the design condition, with an increase in laminar flow extent observed outboard. The design condition experienced a mix of TS- and FB-induced transition due to the method used to set the targets. For the -10% case, the dominant mode of transition was TS, which was caused by a slightly more adverse pressure gradient relative to the design condition. Additionally, some stations experienced a spike in pressure coefficient at the leading edge that caused more significant CF growth than observed for the design condition. However, CF does not exceed the critical N-factor at any station. For the +10% case, the reduction in laminar flow was less pronounced midspan and improvements in laminar flow extents were observed both inboard and outboard. This case exhibited pressure distributions with a more pronounced leading-edge spike in pressure coefficient along with a slightly less adverse rooftop gradient, with FB observed as the dominant mode of transition. Note that even though this case experienced more significant spikes in the pressure coefficient at the leading edge, CF was still not shown to induce transition. Finally, comparing the ±10% $C_{L,design}$ results from Figures 12b and 13, the most significant reduction in benefit is observed for the -10% condition, with a 5.8 count benefit compared to an 8.3 count benefit at the design condition, and a 6.5 count benefit at the +10% condition.
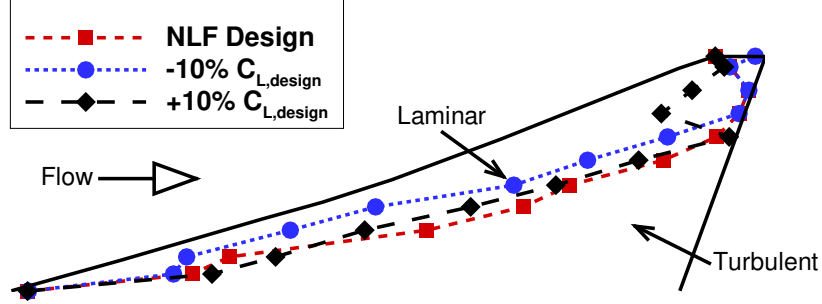
15

Figure 13. Laminar front comparison for design condition and ±10% $C_{L,design}$.

2. Mach Shift

The Mach shift results are shown in Figure 14 for NLF design both with laminar flow and fully turbulent. Figure 14a shows the drag coefficient as a function of Mach number. Note that the angle of attack was adjusted at each Mach number to constrain the lift coefficient to the design value. The drag coefficient for both cases shows a 1-2 count variation over the entire range of Mach number considered. The rise in drag coefficient over the Mach range is slightly more significant for the fully turbulent case. This is confirmed in Figure 14b, which illustrates an increasing benefit with increasing Mach number for the case with laminar flow. The results show a drag count benefit of at least 7.96 counts, with a maximum benefit of 8.44 counts observed at a Mach number of 1.46.
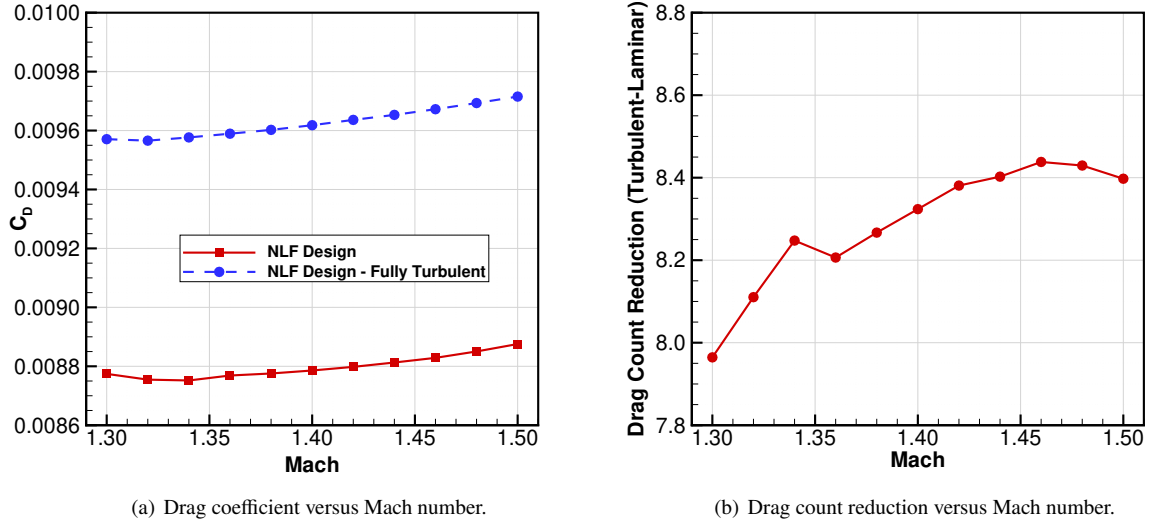

| (a) Drag coefficient versus Mach number. | (b) Drag count reduction versus Mach number. |

Figure 14. Mach shift results for the NLF design simulated both with laminar flow and fully turbulent.

The predicted laminar fronts are illustrated in Figure 15 for Mach numbers of 1.3, 1.4 (design condition), and 1.5. The results show good agreement both inboard and outboard for all three Mach numbers. The primary observation is that the midspan laminar front shifts aft with increasing Mach number. The result is an increase in laminar extent over the span and, as observed in Figure 14b, an increase in the performance benefit with an increase in Mach. For the Mach shift, the dominant transition modes were unchanged from the design condition, with a mix of TS, FB, and transition due to the pressure gradient exceeding the LASTRAC criterion. At the lower Mach numbers, the angle of attack was increased, relative to the design condition, to achieve the design lift coefficient. This led to pressure coefficient spikes at the leading edge. For the higher Mach numbers, the opposite was true and the pressure distributions featuring a slightly less pronounced suction peak. In both cases, the changes in pressure coefficient at the leading edge did not cause CF-induced transition. Relative to the design condition, the results show a decrease in benefit for decreases in Mach number and an increase in benefit for increasing Mach number with a total variation of 0.6 counts for the chosen Mach number range.
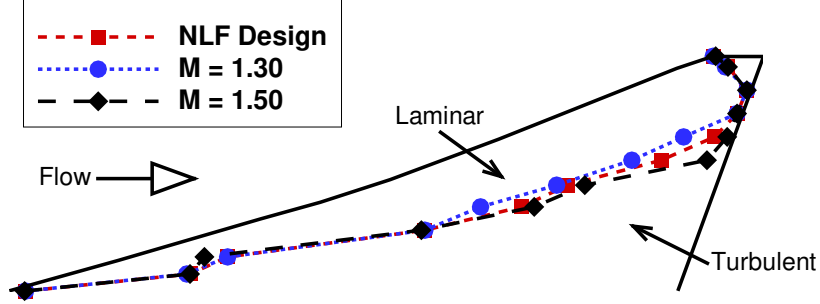
16

Figure 15. Laminar front comparison for Mach 1.3, 1.4 (design condition), and 1.5.

V. Future Work

This preliminary design study is the first step towards the design of an NLF wing for the full configuration to enable an assessment of the impact of the CATNLF pressure target architecture on the sonic boom loudness. This will involve overcoming challenges with interference effects and grid movement near the fuselage-wing juncture. Additionally, attachment line transition will need to be addressed along with the frequency-beta pairs used for the stability analysis. These topics are discussed in the following subsections.

A. Attachment Line Transition/Contamination

The spanwise distributions of Re_θ for both the NLF design and baseline are provided in Figure 16. The results show that the NLF design transitions to turbulent flow at station 2 and does not relaminarize ($Re_\theta < 100$) until station 6. Additionally, station 1 was not designed and does not feature laminar flow. As a result, the inboard 50% of the wingspan is fully turbulent. However, the results show that only a small adjustment in Re_θ is required to meet Poll's criterion ($Re_\theta < 235$). This will be corrected in future research through appropriate reductions in leading-edge radius and/or changes to the inboard sweep angle.
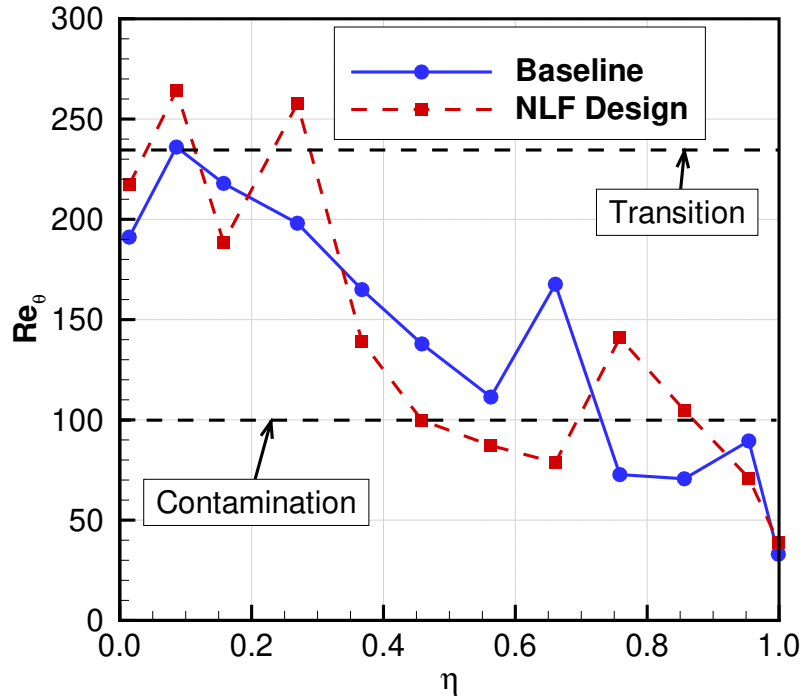

Figure 16. Spanwise distribution of attachment line Re_θ for both the design and baseline.

B. Frequency-Beta Study

As discussed in Section III.D, the stability analyses are performed utilizing 20 frequency-beta combinations to predict the growth of FB instabilities. A study was performed to assess the impact of the frequency-beta sampling density on the growth of FB. This was performed by generating a 50x50 matrix of frequency-beta pairs. The ranges were prescribed by specifying a minimum value and growth rate. For the frequency, the minimum value was chosen to be 5,000 Hz with a growth rate of 8.8%. The minimum value of beta was chosen to be 0.1 with a growth rate of 10.8%. These numbers were chosen to cover the range of frequency and beta included in the original 20 pairs. For each station, a stability analysis was performed for the FB transition mode. An illustration of the frequency-beta pairs for station 7 is provided in Figure 17 along with the corresponding FB curves in Figure 18. The results shown in Figure 17 include the full frequency-beta matrix (FB pairs) along with the original pairs, and both the unstable and critical pairs identified from the stability analysis. For this paper, the unstable modes correspond to any input pair that resulted in FB growth (blue curves in Figure 18) and the critical pairs correspond to combinations that define the FB envelope (red curves in Figure 18). The results illustrate more significant growth of FB using the refined pairs, Figure 18b, relative to the original pairs, Figure 18a.
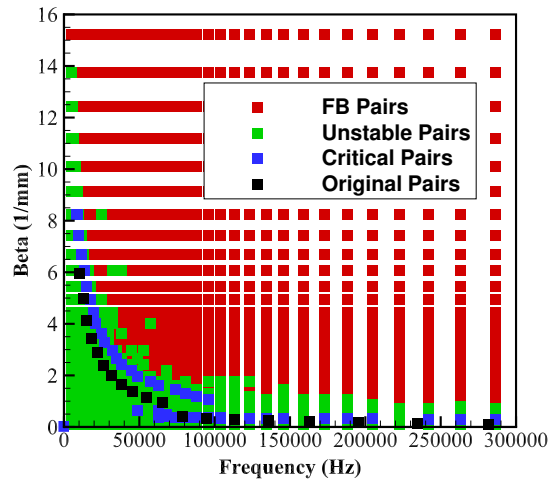

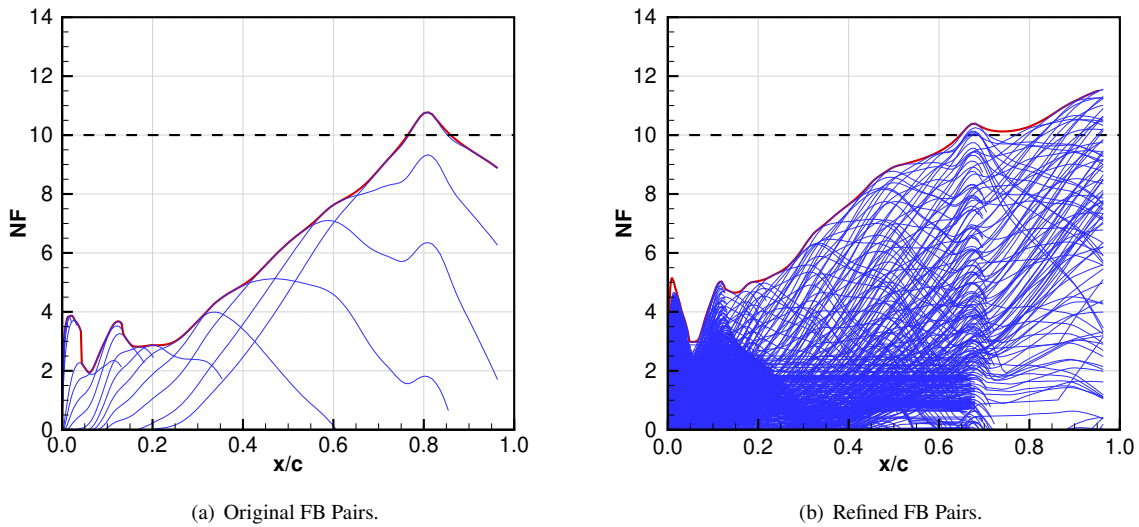**Figure 17. Illustration of frequency-beta pairs for FB study.**

(a) Original FB Pairs.

(b) Refined FB Pairs.

Figure 18. Growth of FB mode predicted using the original and refined pairs at station 4.

Further comparisons of the FB growth are provided in Figure 19, which shows the FB curves for stations 4, 7, and 10 for both the original pairs and the refined pairs. At station 4, the FB growth exceeds the critical N factor at $x/c = 0.65$ for the refined pair while the results using the original pairs do not predict FB growth to exceed the critical N factor. Note that the original stability analysis predicted station 4 to transition at $x/c = 0.42$ due to TS growth. Therefore, the refined pairs do not have an impact at station 4. At station 7, the stability analysis utilizing the original pairs predicts transition to occur at $x/c = 0.77$ due to FB growth. The results from the refined pairs show FB growth exceeding the critical N factor at roughly $x/c = 0.65$, which is a reduction of 12% chord. The results for Station 10 in Figure 19c illustrate more significant growth of FB for the refined pairs. However, station 10 is still predicted to transition due to an excessive pressure gradient in the boundary layer near the trailing edge and no loss of laminar flow is observed for the refined pairs.

(a) Station 4.

(b) Station 7.

(c) Station 10.
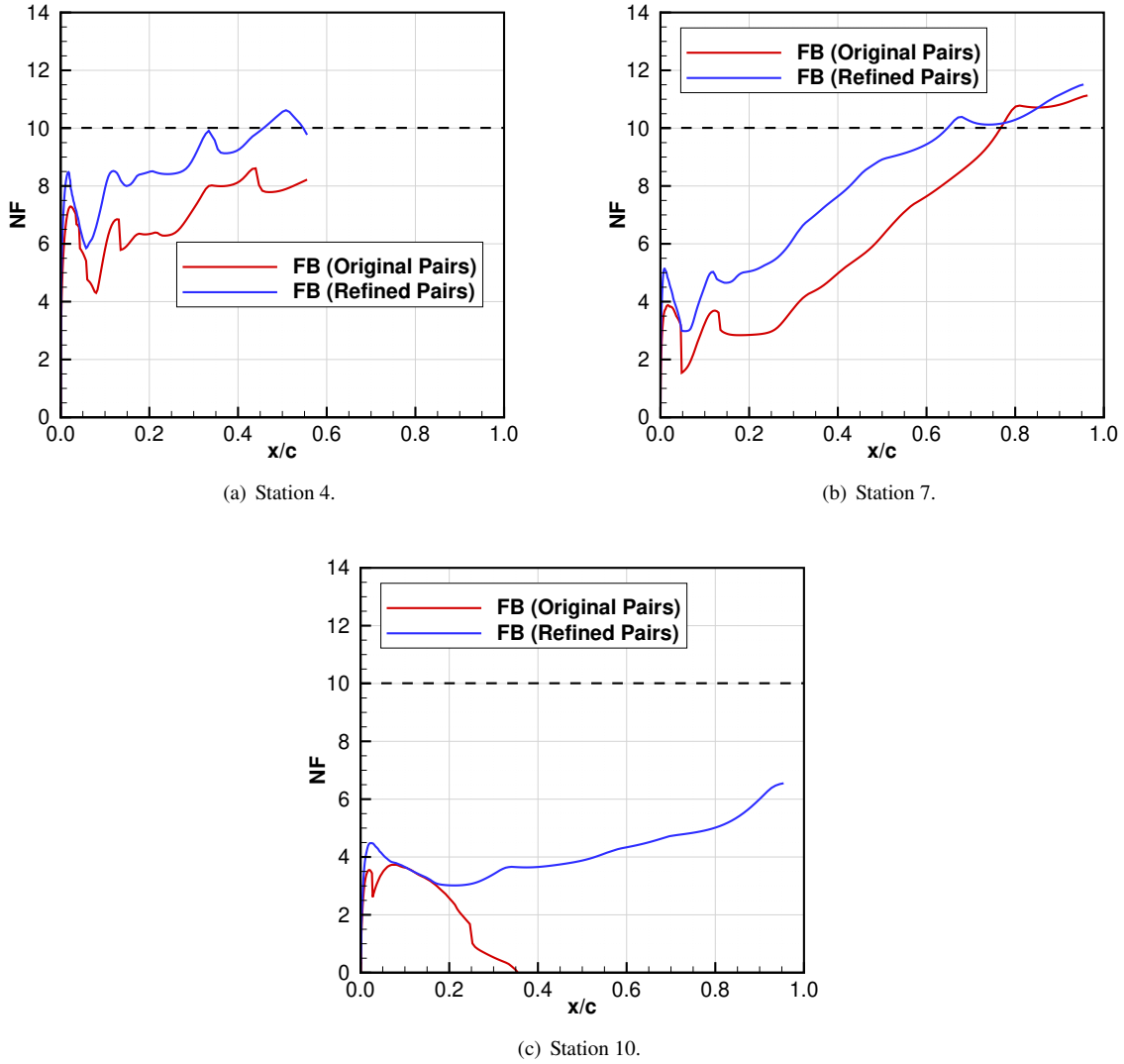
Figure 19. Growth of FB mode predicted using the original and refined pairs at stations 4, 7, and 10.

Figure 20 illustrates the impact of the refined FB pairs on the predicted laminar front. The most significant differences are observed inboard, where stations 2 and 3 are predicted to transition near the leading edge for the refined pairs. Also, a slight shift forward in the front is observed midspan, from stations 4 to 10, for the refined pairs. The laminar front predicted utilzing the refined pairs was used to perform a forced-laminarization simulation using USM3D-ME, which showed a drag count benefit of 6.6 counts compared to the 8.3 count benefit predicted for original pairs. This result

illustrates the significance of correctly choosing the frequency-beta pairs for the stability analysis. Note that the target pressures were chosen based on the original FB pairs, which contributes to the reduction in drag count benefit observed for the refined pairs. Most, if not all, of the drag count benefit should be recovered by utilizing more appropriate FB pairs when defining the pressure targets. This will be addressed in future work.
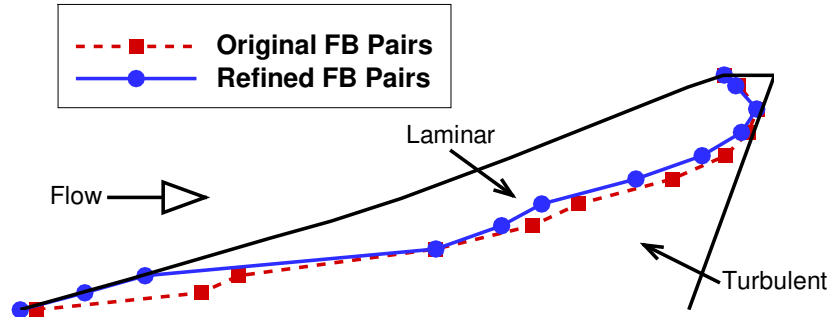

Figure 20. Laminar front comparison for original and refined pairs.

VI. Concluding Remarks

This paper discussed the design of an NLF wing for the C607 low-boom concept, which was a preliminary step towards the ultimate goal of assessing the compatibility of NLF and low-boom. The wing geometry was simplified by removing control surface gaps and bumps. The NLF design process leveraged the CDISC design module coupled to the USM3D-ME flow solver. Additionally, the BLSTA3D and LASTRAC tools were used for transition prediction and the CATNLF method was employed to define the target pressure distributions needed for NLF.

The C607 wing was divided into 12 spanwise stations, with design performed on stations 2 through 11 at the cruise design point of M = 1.4, Re_{MAC} = 33 million, and α = 2.15°. The results show that CF was successfully suppressed at all design stations. The pressure targets were the most challenging to achieve inboard, with better agreement between the design and target pressure distributions observed outboard where the local Reynolds number was the smallest. Overall, the NLF design is predicted to feature laminar flow on 46% of the wing upper surface, which results in a drag count reduction of 8.3 relative to the design analyzed fully turbulent. The angle of attack sweep showed that the NLF design maintains a majority of the drag count reduction for the conditions encompassed by ±10% of $C_{L,design}$. Finally, the Mach shift results show a slight reduction in the proposed benefit for decreases in Mach number with an increase in benefit observed for increases in Mach number. The provided results illustrate the effectiveness of the proposed method for achieving NLF for a highly-swept wing at supersonic speeds.

Future research will extend this work to consider the full configuration to enable an assessment of sonic boom loudness on the ground. This will pose significant challenges including interference effects that could reduce the potential for laminar flow, computational cost from large grids needed to assess boom loudness, and the need to include more restrictive constraints for inclusion of control surfaces and shielding considerations for the top-mounted engine. Additionally, a turbulent design for the C607 will be performed, with the goal of improving performance while simultaneously maintaining or reducing the sonic boom loudness. The turbulent design will enable a more accurate assessment of the performance benefit offered by the NLF design. Other considerations for future work discussed include mitigation of attachment line transition and contamination along with improvements to the transition prediction by defining more dense sampling of the frequency-beta pairs and/or a more sophisticated method of scaling the baseline pairs based on the geometry and flow at the station of interest. These topics will be discussed further in a future publication.

Acknowledgments

References

[1] Joslin, R. D., "Overview of Laminar Flow Control," NASA/TP 1998–208705, 1998.

[2] Gaster, M., "On the Flow Along Swept Leading Edges," *Aeronautical Quarterly*, Vol. 18, No. 2, 1967, pp. 165–184.

[3] Poll, D., "Some Observations of the Transition Process on the Windward Face of a Long Yawed Cylinder," *Journal of Fluid Mechanics*, Vol. 150, 1985, pp. 329–356.

[4] Anderson, B. T., and Meyer Jr, R. R., "Effects of Wing Sweep on In-flight Boundary-layer Transition for a Laminar Flow Wing at Mach Numbers from 0.60 to 0.79," *NASA STI/Recon Technical Report N*, Vol. 91, 1990, p. 24555.

[5] Lynde, M. N., and Campbell, R. L., "Computational Design and Analysis of a Transonic Natural Laminar Flow Wing for a Wind Tunnel Model," *35th AIAA Applied Aerodynamics Conference*, 2017, p. 3058.

[6] Campbell, R. L., and Lynde, M. N., "Building a Practical Natural Laminar Flow Design Capability," *35th AIAA Applied Aerodynamics Conference*, 2017, p. 3059.

[7] Lynde, M. N., and Campbell, R. L., "Expanding the Natural Laminar Flow Boundary for Supersonic Transports," *34th AIAA Applied Aerodynamics Conference*, 2016, p. 4327.

[8] Castner, R. S., Simerly, S., and Rankin, M., "Supersonic Inlet Test for a Quiet Supersonic Transport Technology Demonstrator in the NASA Glenn 8-foot by 6-foot Supersonic Wind Tunnel," *2018 Applied Aerodynamics Conference*, 2018, p. 2850.

[9] Frink, N. T., "Tetrahedral Unstructured Navier-Stokes Method for Turbulent Flows," *AIAA Journal*, Vol. 36, No. 11, 1998, pp. 1975–1982.

[10] Frink, N. T., Pirzadeh, S. Z., Parikh, P. C., Pandya, M. J., and Bhat, M., "The NASA Tetrahedral Unstructured Software System (TetrUSS)," *The Aeronautical Journal*, Vol. 104, No. 1040, 2000, pp. 491–499.

[11] Pandya, M. J., Frink, N. T., Ding, E., and Parlette, E., "Toward Verification of USM3D Extensions for Mixed Element Grids," *31st AIAA Applied Aerodynamics Conference*, 2013, p. 2541.

[12] Pandya, M. J., Diskin, B., Thomas, J. L., and Frink, N. T., "Assessment of USM3D Hierarchical Adaptive Nonlinear Method Preconditioners for Three-Dimensional Cases," *AIAA Journal*, 2017, pp. 3409–3424.

[13] Roe, P. L., "Approximate Riemann Solvers, Parameter Vectors, and Difference Schemes," *J. Comp. Phys.*, Vol. 43, 1981, pp. 357–372.

[14] Spalart, P. R., and Allmaras, S. R., "A One-Equation Turbulence Model for Aerodynamic Flows," *Recherche Aerospatiale*, Vol. 1, 1994, pp. 5–21.

[15] Campbell, R., "Efficient Viscous Design of Realistic Aircraft Configurations," *29th AIAA, Fluid Dynamics Conference*, 1998, p. 2539.

[16] Campbell, R. L., and Lynde, M. N., "Natural Laminar Flow Design for Wings with Moderate Sweep," *34th AIAA Applied Aerodynamics Conference*, 2016, p. 4326.

[17] Wie, Y.-S., "BLSTA: A boundary layer code for stability analysis," Tech. Rep. HTC-9204, 1992.

[18] Chang, C.-L., "The Langley Stability and Transition Analysis Codes (LASTRAC): LST, Linear & Nonlinear PSE for 2D, Axisymmetric, and Infinite Swept Wing Boundary Layers," *41st Aerospace Sciences Meeting and Exhibit*, 2003, p. 974.